



Multi-atom Pt and PtRu catalysts for high performance AEMFCs with ultra-low PGM content

Horie Adabi^{a,1}, Abolfazl Shakouri^{a,1}, Andrea Zitolo^b, Tristan Asset^c, Anastassiya Khan^b, Jasmine Bohannon^a, Raphaël Chattot^c, Christopher Williams^a, Frédéric Jaouen^c, John R. Regalbuto^{a,*}, William E. Mustain^{a,*}

^a Department of Chemical Engineering, University of South Carolina, Columbia, SC 29208, USA

^b Synchrotron SOLEIL, L'orme des Merisiers, BP 48 Saint Aubin, 91192 Gif-sur-Yvette, France

^c ICGM, Univ. Montpellier, CNRS, ENSCM, Montpellier, France

ARTICLE INFO

Keywords:

Low PGM
AEM
Fuel cell
Oxygen reduction
Hydrogen oxidation
Catalyst

ABSTRACT

To reduce the platinum group metal (PGM) loading in anion exchange membrane fuel cells (AEMFCs), it is important to transition to catalysts with very low PGM content, and eventually to catalysts that are completely PGM-free. In this work, four supported low-PGM Pt and PtRu catalysts were prepared using a new, simple, scalable technique: Controlled Surface Tension (CST) method. CST allows for a high density of very small multi-atom clusters. Catalysts were physically characterized using a wide array of techniques and tested for their ORR and HOR activity both ex-situ and integrated into operating AEMFCs. The PGM loading was reduced by a factor of 14 while achieving comparable performance to commercial catalysts. AEMFCs were also assembled with ultralow PGM loading ($0.05 \text{ mgPGM cm}^{-2}$), where PtRu anodes were paired with Fe–N–C cathodes to achieve a specific power of 25 W/mgPGM (40 W/mgPt).

1. Introduction

Anion exchange membrane fuel cells (AEMFCs) are a possible lower-cost drop-in replacement for well-developed and commercialized proton exchange membrane fuel cells (PEMFCs). AEMFCs operate at similar temperatures and pressures as PEMFCs, and their performance and durability have increased significantly in recent years [1–7]. State-of-the-art peak power densities for AEMFCs are 3.5 W cm^{-2} [8] with H_2/O_2 gas feeds and 1.8 W cm^{-2} with H_2/air (CO_2 -free). AEMFCs have also been reported that can be operated stably and continuously for more than 2000 h with less than 5% total voltage decay [9]. The true advantage of AEMFCs over PEMFCs is the opportunity to offer much lower cost [10] by allowing for cheaper materials as membranes, bipolar plates, and electrocatalysts [11,12]. From a catalytic perspective, the lower operating potential in alkaline vs. acid media manipulates the structure of water near the surface of the catalyst, leading to enhanced oxygen reduction reaction (ORR) kinetics. This is expected to allow researchers to reduce the platinum group metal (PGM) loading significantly or allow PGM-based materials to be completely eliminated [13],

and some PGM-free ORR catalysts have already been reported in AEMFCs with power densities as high as 2 W cm^{-2} [13–15]. However, all of the achievements mentioned above – even those with PGM-free cathodes – have been made using AEMFCs with overall high PGM content ($\sim 1 \text{ mgPt cm}^{-2}$) [16,17].

To facilitate the transition of AEMFCs from high-PGM to low-PGM to PGM-free, the U.S. Department of Energy (DOE) recently set several targets for AEMFCs [18]. In these targets, the full cell PGM loading is reduced to 0.2 mg cm^{-2} by 2023, 0.125 mg cm^{-2} by 2024, and zero PGM by 2030. The near-term DOE targets can be met by reducing the loading of existing catalysts, which can be accomplished by maximizing dispersion and metal utilization [19]. One effective strategy is to do this is to create atomically-dispersed catalysts, which can take the form of single atoms or small multi-atom clusters [19–21].

Unfortunately, a scalable method for the creation of single atom or multi-atom cluster catalyst is not yet available. One of the most widely used synthesis methods in industry today is dry impregnation (DI) (also known as incipient wetness impregnation), because it requires few steps and can be done rapidly and economically at the kg scale. DI uses a small

* Corresponding authors.

E-mail addresses: regalbuj@cec.sc.edu (J.R. Regalbuto), mustainw@mailbox.sc.edu (W.E. Mustain).

¹ Indicates equal contribution.

amount of water (typically equal to the titrated pore volume of the support) to dissolve the catalyst precursor. Water can dissolve most industrial precursors because it has the highest polarity among all conventional solvents [22]. However, it has been reported that the capillary effect caused by the high surface tension of water causes agglomeration of the precursors upon drying; this process is illustrated in Fig. 1a. Precursor agglomeration during drying intrinsically leads to the formation of large nanoparticles [23]. One of the ways to overcome the limitations of DI is to control the surface charge of the support, which is the underlying principle behind the strong electrostatic adsorption method [24,25], though the resulting catalysts using that method and others is typically smaller nanoparticles, not single atoms or multi-atom clusters.

One approach to create ultra-small catalyst structures is to reduce the surface tension of the solvent phase during synthesis. Reducing the surface tension will minimize the capillary effect, resulting in a higher number of smaller solvent droplets (as opposed to a smaller number of larger droplets in DI). Smaller droplets means fewer precursors in intimate contact during synthesis, leading to a much better dispersion of single-atoms and clusters. An illustration of this controlled surface tension (CST) method and its comparison with DI is provided in Fig. 1. In the CST method, the surface tension of the precursor solution is reduced by introducing a second polar solvent with lower surface tension, e.g., acetone. The mixing of water and acetone will not only alter the surface tension of the solution; the difference in physical properties between the two solvents also triggers the Marangoni effect, spontaneously mixing the synthesis media throughout the pores [26]. In metallic structures, this will mean a more homogeneous composition throughout. Reducing the surface tension of the solution also reduces the contact angle of the solvent droplets upon drying, allowing for the formation of ultra-small precursor crystallites (Fig. 1b).

In this work, CST-synthesized Pt and PtRu clusters are prepared on two supports: Vulcan XC-72R (VC, Cabot Corp.) and N-doped mesoporous carbon (NC, Pajarito Powder, ECS-003701). The catalysts are extensively physically characterized by Cs aberration-corrected scanning transmission electron microscopy (STEM), extended X-ray absorption fine structure (EXAFS), and X-ray Absorption Near-Edge Structure (XANES). It is shown that these supported Pt and PtRu

catalysts are quite active for the oxygen reduction reaction (ORR) and hydrogen oxidation reaction (HOR), respectively, which is shown not only in ex-situ tests, but the catalyst is also integrated into state-of-the-art AEMFC electrodes, enabling record performance to be achieved. Finally, AEMFCs with ultra-low PGM loading (0.05 mg cm^{-2}) are assembled and tested, with the goal of surpassing the U.S. Department of Energy 2022 performance target for AEMFCs: initial performance of 0.65 V at 1.0 A cm^{-2} with H_2/O_2 reacting gases, temperature $\geq 80^\circ\text{C}$; pressure $\leq 150 \text{ kPa}$ and total PGM loading $\leq 0.2 \text{ mg cm}^{-2}$.

2. Experimental

2.1. Synthesis of 5 wt% DI-Pt/VC, DI-PtRu/VC and DI-PtRu/NC

DI is widely used in industrial catalyst synthesis. The process starts by titrating with water to find the pore volume of the support material. Then, a predetermined amount of metal precursor (e.g. H_2PtCl_6 for a Pt catalyst) is dissolved in a particular volume of water equal to the support's titrated pore volume. The precursor solution and the support are well mixed and dried overnight. The resulting dry powder is then heat treated in a reducing atmosphere to yield the catalyst.

DI catalysts were prepared by dissolving H_2PtCl_6 and $(\text{NH}_4)_2\text{RuCl}_6$ precursors at their desired ratio in a volume of $18.2 \text{ M}\Omega$ deionized water that was equal to the pore volume of the VC or NC support. The support and precursor solution were added to a centrifuge tube and well mixed by vortex mixer at 3000 rpm for 2 min . The mixture was a thick slurry, which indicated that a majority of the precursor solution was taken up into the support. The slurry was then placed in a fume hood and allowed to dry overnight. Lastly, the dried powder was put into a tube furnace and heat treated at 170°C in a $10\%/90\%$ H_2/N_2 atmosphere. The full details about these catalysts, and all other catalysts used in this work, including their metal loadings, are provided in Table S1.

2.2. Synthesis of 5 wt% CST-Pt/VC, CST-Pt/NC, CST-PtRu/VC, and CST-PtRu/NC

The catalysts synthesized using the CST method followed a similar procedure as DI except for steps added before drying. The precursor

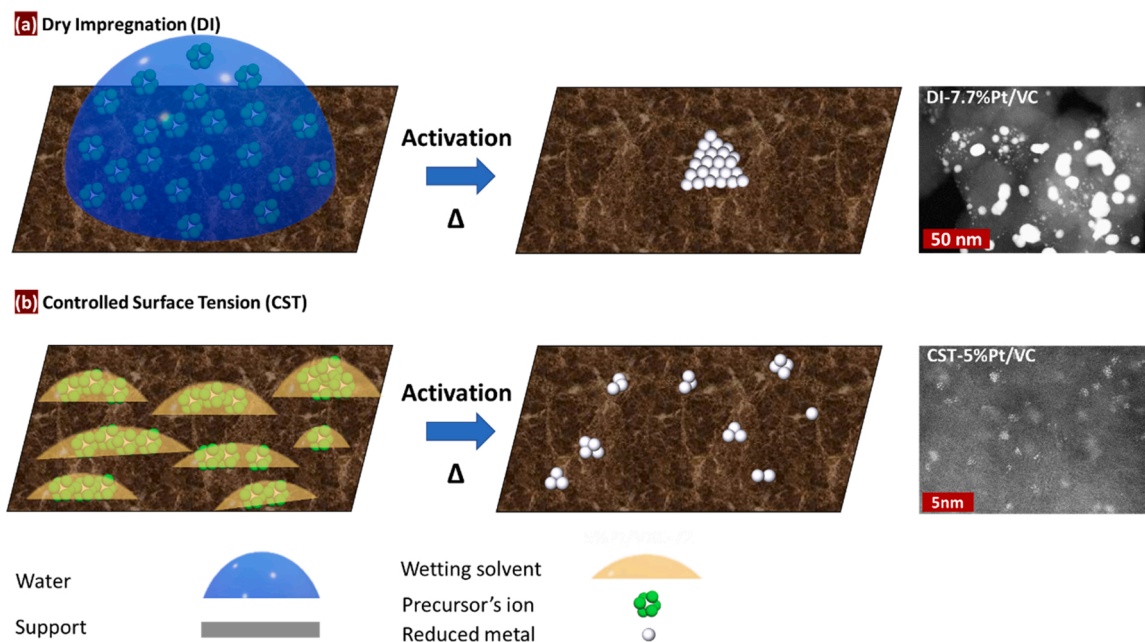


Fig. 1. Effect of local surface tension during drying on the resulting catalyst structure. Catalyst prepared by: a) dry impregnation (DI) where the high surface tension of water results in large droplets upon drying, b) controlled surface tension method (CST) which reduces the surface tension of the synthesis media by addition of a wetting solvent (e.g. acetone) in the same volume as water to form ultrasmall droplets upon drying. Catalysts were reduced under $10\% \text{ H}_2$ (balance N_2) at 170°C .

solution and support were mixed in a centrifuge tube using vortex mixer at 3000 rpm for 2 min. The volume of deionized water to form the solution was again equal to the pore volume of the VC or NC support. After obtaining a uniform thick slurry, acetone (as the wetting solvent) with same volume as water was added to the centrifuge tube and mixed for another 2 min at 3000 rpm. The catalyst-water-acetone slurry was transferred immediately into a crucible boat and placed inside a 1-inch tube furnace. After entering the furnace, the slurry was first dried at 50 °C for 30 min under flow of 10%/90% H₂/N₂. After the drying step, the temperature was ramped up to 170 °C at a rate of 2 °C/min. The catalysts were held at 170 °C for one hour, after which they were cooled down to room temperature.

It should be noted that each catalyst was made and tested several times to ensure repeatability and the results presented here are truly representative. In fact, the CST catalysts here were made at least 5 times, having the same structure and properties each time.

2.3. Electron microscopy

An imaging JEOL 2100 F 200 kV scanning transmission electron microscope (STEM) equipped with a CEOS Cs corrector on the illumination system was used to characterize the catalyst via Z-contrast imaging. High angle annular dark-field (HAADF) STEM images were captured with a Fischione Model 3000 HAADF detector with a camera length such that the detector spanned 50–250 mrad. The scanning acquisition was synchronized to 60 Hz A.C. electrical power to minimize 60 Hz noise in the images, and a pixel dwell time of 15.7 μs was chosen. To prepare the sample for imaging, the catalyst was suspended in IPA and dispersed using ultrasonic vibration for 1 min. Then, a droplet of the suspension was placed on the holey carbon-coated (mesh 200, SPI Inc.) copper TEM grid on a platinum ring. A filter paper underneath the TEM grid absorbed the liquid that passed through the carbon-coated TEM grid. The sample was cleaned using an electron beam shower under vacuum for 15 min to clean the surface of chemical residue.

2.4. XAS data collection

Pt L₃-edge and Ru K-edge X-ray absorption spectra were collected in fluorescence mode at room temperature at the SAMBA beamline of the Synchrotron SOLEIL, using a sagittal focusing double-crystal monochromator equipped with Si(220) crystals, and with a Canberra 35-elements monolithic planar Ge pixel array detector. The samples were prepared as inks by ultrasonically mixing 10 mg of catalyst with 50 μL of de-ionized water and 100 μL of 5 wt% Nafion™ dispersion (DuPont). A 50 μL aliquot was then pipetted on ~3 cm² circular area of a 100 μm-thick graphite foil (Goodfellow cat. C 000200/2) and installed in a customized electrochemical cell [27] with N₂ saturated 0.1 M NaOH electrolyte.

2.5. Electrochemical measurements

All electrochemical measurements were performed on a thin-film rotating disk electrode (RDE) or rotating ring disk electrode (RRDE) in a customized three-electrode cell that was made by Adams & Chittenden Scientific Glass. A platinum mesh was used as the counter electrode and a double junction Ag/AgCl was the reference electrode (Pine Research Instrumentation, 4 M aqueous KCl internal solution) [28]. To study the ORR, cyclic voltammograms were collected with N₂ and O₂ saturated electrolyte using an Autolab PGSTA302N potentiostat. The working electrodes were made by first creating an ink and then depositing that ink onto the glassy carbon RRDE disk (E6R2 Fixed-Disk RRDE Tips PEEK, Pine Research Instrumentation, Pt ring, disk geometric surface area: 0.237 cm²). This was done for synthesized DI-Pt/VC, CST-Pt/VC, CST-Pt/NC and Fe-N-C[29] catalysts. 8.5 μL of ink with the following composition were deposited onto the electrode: 5 mg of catalyst, 744 μL of IPA, 92 μL of DI water, and 54 μL of 5 wt% Nafion ionomer dispersion

(DuPont). The pH of the ink was adjusted to 10 by adding a small amount of 0.1 M KOH. For commercial Pt/VC (denoted as Com-Pt/VC; Alfa Aesar HiSPEC 4000, Pt nominally 40 wt%, supported on Vulcan XC-72R carbon) working electrodes, the procedure was slightly different. There, 4.2 μL of a catalyst ink with the following composition was deposited onto the electrode: 2.5 mg catalyst, 744 μL IPA, 92 μL DI water and 54 μL 5 wt% Nafion ionomer dispersion (DuPont). All of the films were dried at room temperature on a gravity leveled inverted rotator spun at 700 rpm. Prior to thin-film deposition, the glassy carbon electrodes were polished with a 0.05 μm alumina suspension and carefully washed with 18.2 MΩ cm Millipore ultrapure water (UPW) and dried in air for 20 min. The three-electrode cell was washed using the UPW and aqueous 0.1 M KOH before use (10 times and 5 times, respectively) [28].

To measure the ORR activity, the disk electrode was rotated at 1600 rpm in O₂-saturated 0.1 M KOH and the voltage was scanned at a rate of 20 mV s⁻¹ between 0.2 V and 1.05 V vs RHE. The ring electrode potential was set to 1.1 V vs. RHE. The hydrogen peroxide yield (%) (H₂O₂) and electron transfer number (*n*) were calculated by the Eqs. (1) and (2), respectively [30].

$$H_2O_2\% = 200 \times \frac{i_r}{i_d + \frac{i_r}{N_c}} \quad (1)$$

$$n = 4 \times \frac{i_d}{i_d + \frac{i_r}{N_c}} \quad (2)$$

Where *n* is the average number of electrons transferred per reacting oxygen, *i_d* is the disk current, *i_r* is the ring current, and *N_c* is the collection efficiency of the RRDE (*N_c* = 0.38). At each potential, Eq. (3) was used to determine the kinetic current density. The kinetic current at 0.9 V was used to find the mass activity of the catalyst from Eq. (4) [31].

$$I_K = \frac{I_{lim}(A) \times I(A)}{I_{lim}(A) - I(A)} \quad (3)$$

$$MassActivity = \frac{I_K}{m} \quad (4)$$

Where *I_k* is the kinetic current and *I_{lim}* is the measured mass transport limiting current.

To study the HOR, the overall procedure and tools were similar to ORR, except for a few changes. Cyclic voltammograms were collected with N₂ and H₂ saturated electrolyte using an Autolab PGSTA302N potentiostat. The working electrodes were prepared by depositing a catalyst thin film onto a RDE glassy carbon disk (E6R2 Fixed-Disk RRDE Tips PEEK, Pine Research Instrumentation, Pt ring, disk geometric surface area: 0.196 cm²). This was done for synthesized DI-PtRu/NC, CST-PtRu/VC, and CST-PtRu/NC catalysts by dropping 8.5 μL of an ink with the following composition onto the electrode: 5 mg of catalyst, 744 μL of IPA, 92 μL of DI water, and 54 μL of 5 wt% Nafion™ ionomer dispersion (DuPont). The pH of the ink was adjusted to 10 by adding a small amount of aqueous 0.1 M KOH. For commercial PtRu/VC (denoted as Com-PtRu/VC; Alfa Aesar HiSPEC 4000, Pt nominally 40 wt%, Ru, nominally 20 wt% supported on Vulcan XC-72R carbon) working electrodes, the procedure was slightly different. There, 4.2 μL of a catalyst ink with the following composition was deposited onto the electrode: 2.5 mg catalyst, 744 μL IPA, 92 μL DI water and 54 μL 5 wt% Nafion ionomer dispersion (DuPont).

To determine the HOR activity, the electrode was rotated at 1600 rpm in H₂-saturated 0.1 M KOH. The potential was scanned linearly at a rate of 20 mV s⁻¹ from -0.05–0.25 V vs RHE. To determine the HOR mass activity, the current was read at a potential of 0.2 vs. NHE, which was then divided by the mass of the catalyst on the working electrode.

The electrochemically active surface area (ECSA) was determined by cyclic voltammetry (CV), where the electrode potential was scanned

from -0.05 – 0.25 V vs RHE at a rate of 50 mV s^{-1} in N_2 -saturated 0.1 M KOH . From the CV's, the charge related to hydrogen underpotential deposition was calculated and the ECSA was found by Eq. (5) [31]:

$$ECSA_{PGMcat(m^2 g_{PGM}^{-1})} = \left[\frac{Q_{H-adsorption}(C)}{210 \mu C_{cmPGM}^{-2} L_{PGM} (mg_{PGM} cm^{-2}) A_g (cm^2)} \times 10^5 \right] \quad (5)$$

Where the catalysts electrochemical surface area ($ECSA_{Pt,cat}$) is reported in $m^2 g_{PGM}^{-1}$; Q_H is the charge for full coverage for clean polycrystalline PGM, L_{PGM} is the working electrode PGM loading ($mg_{PGM} cm^{-2}$) and A_g (cm^2) is the geometric surface area of the glassy carbon electrode (0.196 cm^2).

2.6. GDE fabrication and AEMFC testing

To prepare anode and cathode gas diffusion electrodes (GDEs), inks were prepared from a combination of the catalyst powder, ionomer powder, and solvent [2,32]. The cathode catalyst was either CST-Pt/VC, CST-Pt/NC or Com-Pt/VC. The anode catalyst was either CST-PtRu/VC, CST-PtRu/NC or Com-PtRu/VC. Ink preparation began by hand-grinding a powdered poly(norbornene) tetra block copolymer ionomer [9] in a mortar and pestle for 10 min. Next, 200 mg of catalyst and 1 mL of UPW was added to the mortar and ground for 10 min, forming a homogenous slurry. The AEI powder mass comprised 20 wt% of the total solid mass of all of the catalyst layers in this paper. Then, 1.5 mL of isopropyl alcohol was added into the mortar, and the thinning mixture was homogenized by another 5 min of grinding. A final 5 mL of IPA was added to the mortar, and the final ink was transferred to a PTFE-

lined vial and sonicated for 1 h in an ice bath. The ink was sprayed onto a Toray TGP-H-60 gas diffusion layer (5 wt% PTFE wet proofing) using an air-assisted sprayer (Iwata) to fabricate gas diffusion electrodes (GDEs). It should also be noted that additional carbon and PTFE (8 wt%) were added to the anode catalyst layers to obtain a AEI:C:Pt ratio of 0.417:1.5:1 [9].

To convert the counter ion for the quaternary ammonium groups in the polymers from the bromide to the hydroxide form, the anode GDE, cathode GDE, and anion exchange membrane (AEM) were hydrated in $18.2 \text{ M}\Omega$ deionized water for 20 min and then soaked three times in 1.0 M KOH . The AEM in all tests was a $20 \mu\text{m}$ -thick poly(norbornene)-based tetrablock copolymer membrane with an ion-exchange capacity of 3.88 meq g^{-1} [33]. The membranes and GDEs were not hot pressed together. They were assembled immediately after functionalization, removing excess KOH , in 5 cm^2 active area Scribner cell with single channel serpentine flow fields. To maintain a pinch of around 25%, $152 \mu\text{m}$ (6 mil, 0.006") and $203 \mu\text{m}$ (8 mil, 0.008") Teflon gaskets were used at the anode and cathode, respectively. The AEMFCs were controlled by a Scribner 850e fuel cell test station. After a break-in procedure, the relative humidity (RH) of both the cathode and anode reacting gases were adjusted to optimize the cell performance at the cell operating temperature (80°C). The gases used in this study were ultra-high purity (UHP) H_2 , UHP O_2 and simulated CO_2 -free air (a mix of UHP N_2 and O_2) from Airgas.

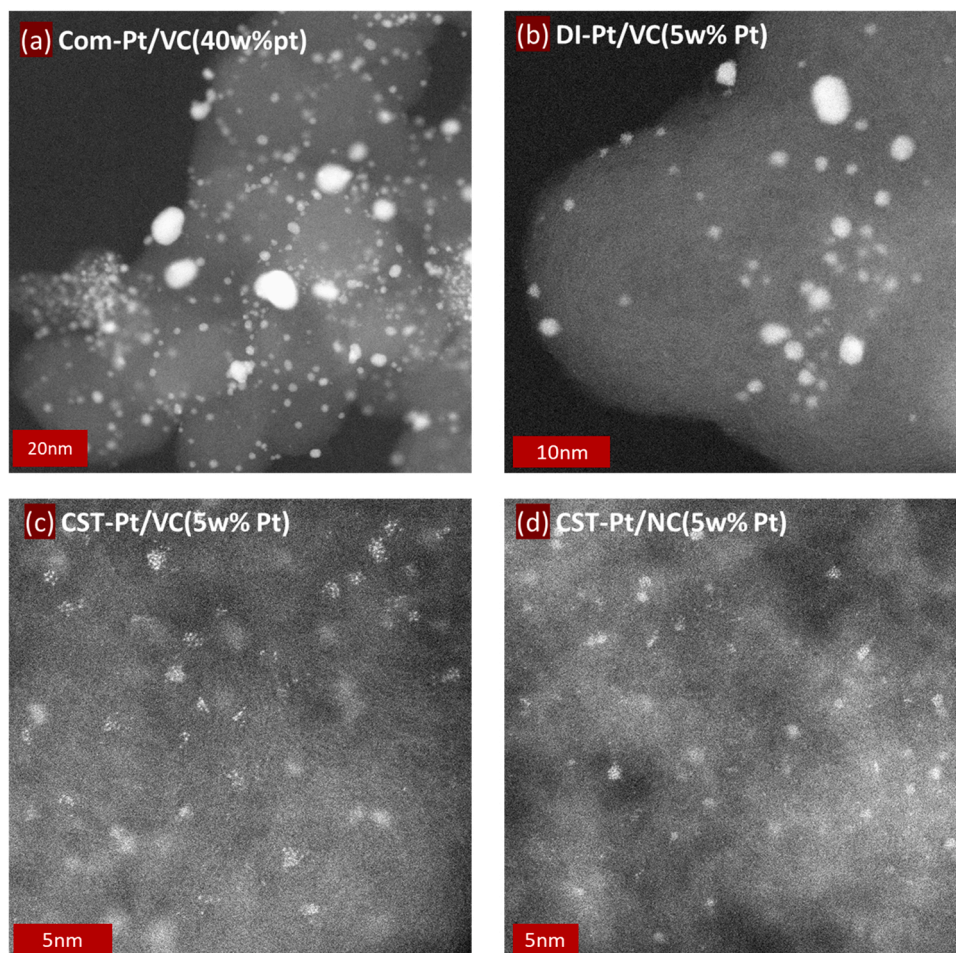


Fig. 2. STEM Images of the supported Pt catalysts. a) 40 wt% Com-Pt/VC; b) 5 wt% DI-Pt/VC; c) 5 wt% CST-Pt/VC; and d) 5 wt% CST-Pt/NC.

3. Results and discussion

3.1. Atomic distribution of Pt and Ru atoms

Fig. 2a shows a representative STEM image of a common 40 wt% carbon-supported Pt commercial catalyst, Com-Pt/VC. It contains large Pt nanoparticles formed on the outer surface of the support. The average Pt particle size for the commercial catalyst was 4.2 nm, as shown in the quantitative particle size distribution in Table S2 and Fig. S1a in the Supporting information. There was a wide dispersion of particle sizes from ~1 nm up to 10's of nm. The very large particles can sacrifice metal utilization, increasing the required loading and cost of AEMFC electrodes, cells and systems.

The first catalyst that was produced in this work was a 5 wt% DI-Pt/VC (Fig. 2b). It was prepared by DI, which is likely similar to production method for the commercial catalyst. Therefore, DI-Pt/VC is meant to be a benchmark catalyst to show how a lower-loading commercial catalyst would behave. The DI-Pt/VC catalyst had a very similar particle size distribution to the commercial catalyst (Table S2 and Fig. S1 in the Supporting Information), though, because of its lower metal loading, complete coverage of the outer surface of the support was not observed and there were not as many large particles.

An analogous 5% Pt supported on VC-72R (CST-Pt/VC) was also prepared by CST. As expected, by altering the surface tension of the synthesis media, the size distribution of the resulting Pt clusters was reduced. This is shown in the STEM images in Fig. 2c as well as the size distribution in Table S2 and Fig. S1 in the Supporting Information. Another interesting note is that manipulating the interaction between

the support and solvent during synthesis allowed the atomic clusters to access the micropores of the support. Hence, the catalyst is distributed throughout the VC, not just on the surface. Unfortunately, it has been reported that due to their small size, around 30% of the micropores in VC can be inaccessible during AEMFC operation [34–37]. To resolve this issue, VC was replaced by mesoporous NC from Pajarito powder. The surface area of this NC support is 800 m²/g and the pore structure is distributed mainly as mesopores and macropores (Figs. S3 and S4 in Supporting Information). A representative STEM image of 5 wt% CST-Pt/NC is shown in Fig. 2d. It also showed very homogenous, atomically-dispersed Pt clusters.

Supported PtRu bimetallic catalysts have been shown to be very effective catalysts for the HOR in alkaline media and AEMFCs [38,39]. A STEM image of a common 60 wt% commercial carbon supported PtRu catalyst (1:1 at. ratio, ~2:1 mass ratio) is shown in Fig. 3a. In that catalyst, very large Pt and Ru particles covered the outer surface of the VC support. Because of high catalyst loading, the largest agglomerates approach 100 nm in size, meaning that many of the Pt and Ru atoms are completely inaccessible to facilitate the HOR. Additionally, it was observed that Pt and Ru are not fully alloyed, but exist primarily as separated particles, mostly existing independently on the support. This was also true for the 6 wt% DI-PtRu/VC prepared internally by DI, Fig. 3b, though the primary particle size and agglomerates were much smaller than the commercial catalyst (comparing Fig. S2a and b in the supporting information).

To maximize the bimetallic effects of the active centers, proximity of the active centers is key to facilitate the HOR. The primary explanations for why PtRu works better in AEMFCs than Pt rely on Ru modifying the

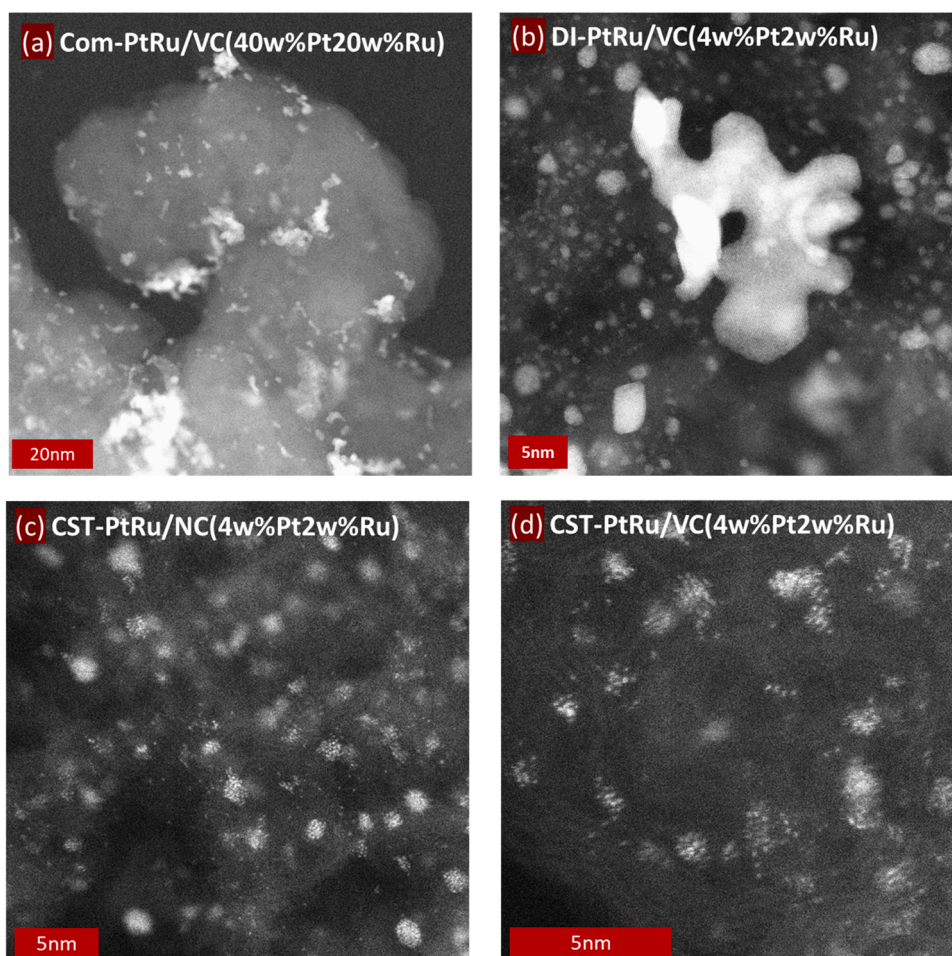


Fig. 3. Representative STEM images for supported PtRu catalysts. a) 60 wt% Com-PtRu/VC; b) 6 wt% DI-PtRu/VC; c) 6 wt% CST-PtRu/NC; d) 6 wt% CST-PtRu/VC.

work function of Pt [1,40,41]. This can be facilitated by the creation of smaller structures with good metal-metal incorporation. Small structures can also improve catalyst accessibility to reactants. To avoid agglomeration and the formation of large particles, while encouraging a more homogenous distribution of Pt and Ru, CST was used to create two supported PtRu catalysts: 6 wt% CST-PtRu/NC (4%Pt-2%Ru) and 6 wt. % CST-PtRu/VC (4%Pt-2%Ru). Representative STEM images for those catalysts are shown in Fig. 3c and Fig. 3d, respectively. The STEM images show that the Pt atoms (brighter) and Ru atoms (less bright) existed together in the clusters in close proximity. This was enabled by the Marangoni effect during synthesis, which provides a well-mixed media that results in atomically mixed clusters. The structures were much smaller than those produced at the same mass fraction by DI as shown in Fig. S2, and CST was able to produce ultra-small and uniformly distributed catalysts. Just like the supported Pt catalysts, the pore structure of the supported PtRu catalysts was the main difference

between the VC and NC-supported low-loading catalysts.

Fig. 4a and b show the comparison between the experimental x-ray absorption near edge structure (XANES) spectra at the Pt L₃- and Ru K-edges of the CST-PtRu/NC catalysts and the metallic foils and oxides references. While the position of the threshold energy of the PtRu catalyst exhibits a slight shift to higher energies relative to the bulk Pt and Ru (which is indicative of a certain degree of oxidation), a strong oxidation of the Pt and Ru metallic sites can be ruled out from comparison with PtO₂ and RuO₂. The spectra indicated a predominantly metallic state of Pt and Ru centers. Extended X-ray absorption fine structure (EXAFS) oscillations in k space are in phase with Pt and Ru metal standards at each absorption edge (Fig. 4c and d), demonstrating that there was no sign of alloying or structural interaction between Pt and Ru. This is not surprising as the post-deposition activation step in CST was carried out at mild thermal conditions (170 °C), which is not sufficient (350 °C [42]) to form Pt-Ru alloys. Therefore, the atoms here

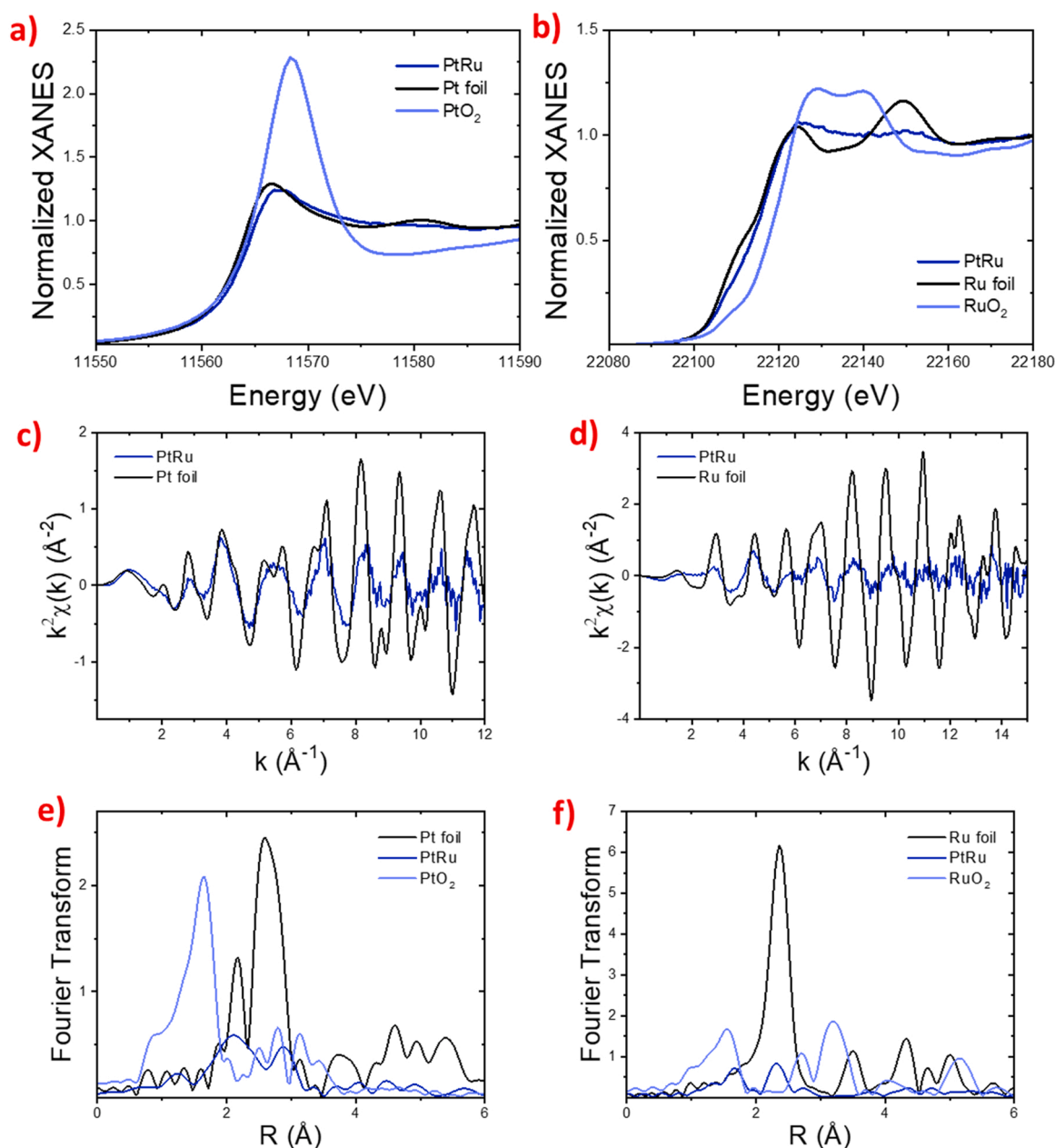


Fig. 4. Understanding the interaction between Pt and Ru in CST-PtRu/NC catalyst. Experimental XANES spectra of (a) CST-PtRu/NC, Pt foil, and PtO₂ at the Pt L₃-edge and (b) PtRu, Ru foil, and RuO₂ at the Ru K-edge (c) PtRu and Pt foil at Pt L₃-edge, and (d) PtRu and Ru foil at Ru K-edge. Non phase-shift corrected Fourier transform of the experimental EXAFS spectra of (e) Pt foil, PtRu, and PtO₂ at Pt L₃-edge, and (f) Ru foil, PtRu, and RuO₂ at Ru K-edge.

should only exist in proximity to one another and may not directly modify the electronic properties of one-another. The amplitude of the EXAFS signals of the PtRu catalysts were reduced compared to that of bulk Pt and Ru, which is due to the very small size of the metal clusters. [43–45] Comparison of the Fourier transform (FT) of the EXAFS signals of PtRu catalysts with PtO₂ and RuO₂ references allows the presence of Pt–O and Ru–O bonds to be excluded (Fig. 4e and f), as well as the existence of PtNx and RuNx moieties, whose FT-EXAFS peaks would be located at about 1.5 Å (not corrected for phase shift).

3.2. Ex-situ electrochemical measurements

The activity and selectivity of the CST-Pt/VC, CST-Pt/NC, DI-Pt/VC, and Com-Pt/VC catalysts towards the ORR were investigated in O₂-saturated 0.1 M KOH. Cyclic voltammograms for all three catalysts are shown in Fig. 5a. The CVs show well-defined ORR reduction peaks between 0.8 and 0.9 V vs. RHE. CST-Pt/NC showed the highest double-layer current due to its much higher surface area than the other supports. In the RRDE polarization curves at 1600 RPM, Fig. 5b, the half-wave potential for the CST-Pt/NC catalyst was about 0.865 V, which is close to Com-Pt/VC even though the latter had a significantly higher loading. The better comparison is with DI-Pt/VC (Fig. S5a), which has a similar loading to CST-Pt/NC, but with particles that have poorer

dispersion. As Fig. S5a shows, the half wave potential for DI-Pt/VC was much lower, indicating that the activity of DI-Pt/VC is far less than CST-Pt/NC. The low potential regime was also affected with DI-Pt/VC, suggesting that there was some mass transport issues with that catalyst as well. The results in Fig. 5b suggest that CST-Pt/NC is well-active for the ORR in alkaline media, with a half wave potential (and hence overall activity) just slightly lower than the commercial catalyst despite having a small fraction of the noble metal. However, it is well established that the half-wave potential alone is not a perfect measure for powder catalysts [14] because loading effects can have a substantial impact on how the data is interpreted. A better comparison between the catalysts is typically the mass-specific or area-specific activity. The mass activity at 0.9 V vs. RHE for the Com-Pt/VC catalyst was 113 A g_{Pt}^{−1} (Fig. 5c), while it was 99 A g_{Pt}^{−1} for CST-Pt/VC and 230 A g_{Pt}^{−1} for the CST-Pt/NC. The DI-Pt/VC had the lowest activity. In fact, its onset potential was so low (Fig. S5a in Supplementary Information) that a mass activity could not be reliably calculated at 0.9 V vs. RHE. These shows that CST-Pt/NC had a much better Pt utilization than the commercial catalyst.

Fig. 5b shows linear sweep voltammograms (20 mV s^{−1}) for CST-Pt/NC carried out at several different rotation rates between 400 and 2500 RPM. This was done in order to calculate the H₂O₂ yield and the average number of electrons transferred (*n*), Fig. 5d. The average value for *n* was 3.94 over the entire potential window and the yield of H₂O₂ was less

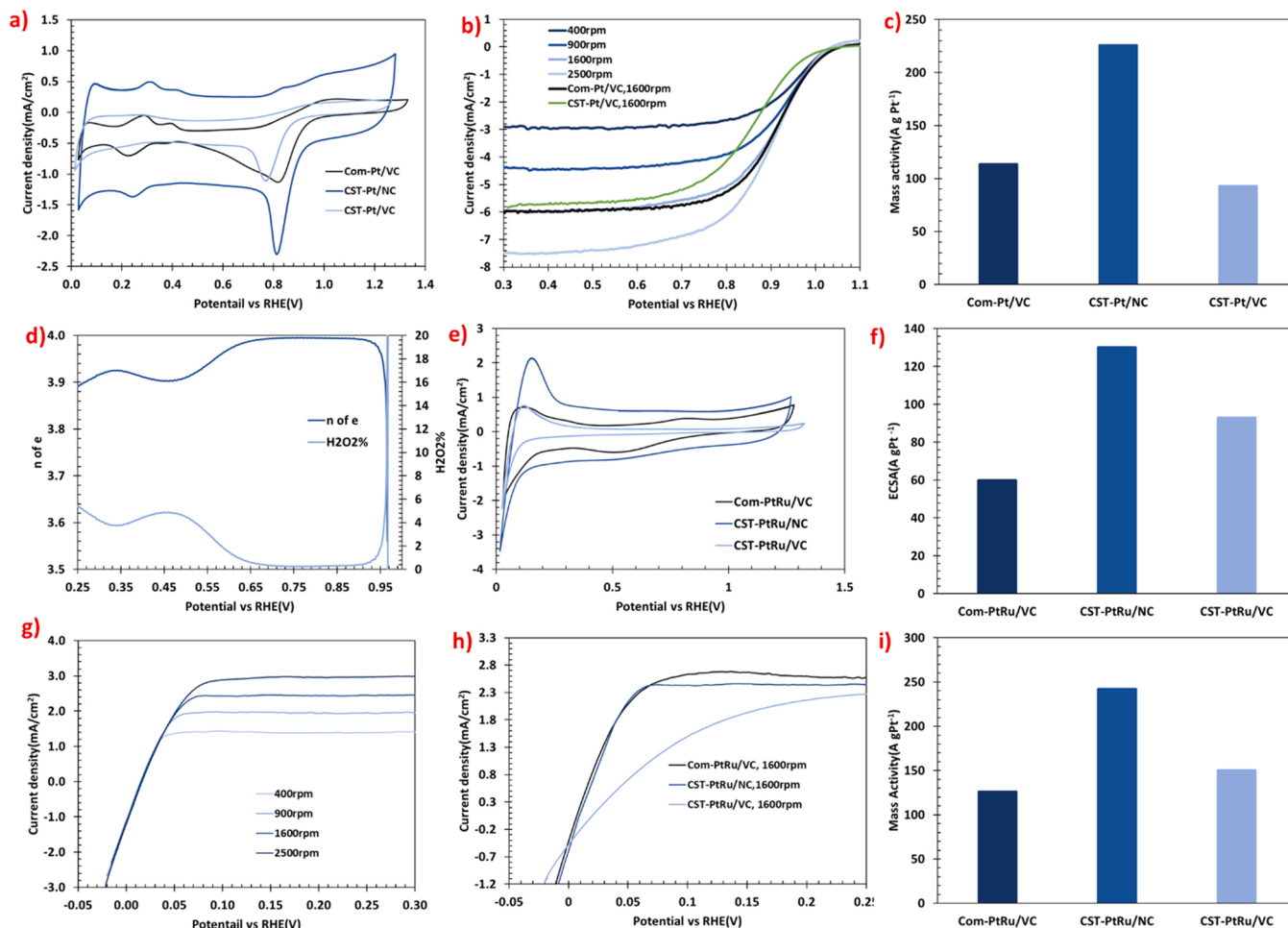


Fig. 5. HOR and ORR Activities for CST, DI and Com catalysts. a) Cyclic voltammograms for CST-Pt/NC, CST-Pt/VC and Com-Pt/VC in O₂-saturated aqueous KOH (0.1 M) electrolyte at a scan rate of 50 mV s^{−1} at room temperature. b) ORR linear sweep polarization curves (20 mV s^{−1}) for CST-Pt/NC in O₂-saturated aqueous KOH (0.1 M) electrolyte at various rotation rates, c) ORR mass activity for the various ORR catalysts. d) Number of electrons (*n*) transferred per O₂ molecule and yield of hydrogen peroxide (H₂O₂%) on the CST-Pt/NC catalyst as a function of potential over the entire experimental range, e) Cyclic voltammograms for CST-PtRu/NC, CST-PtRu/VC and Com-PtRu/VC in N₂-saturated aqueous KOH (0.1 M) electrolyte at a scan rate of 50 mV s^{−1} at room temperature. f) ECSA for the HOR catalysts. g) HOR linear sweep polarization curves (20 mV s^{−1}) for CST-PtRu/NC in H₂-saturated aqueous KOH (0.1 M) electrolyte at various rotation rates h) HOR linear sweep polarization curves (20 mV s^{−1}) for the HOR catalysts at 1600 rpm. i) HOR mass activity at 0.2 V.

than 4%. Most importantly, between 0.6 and 1.0 V (the voltage range at which the cathode would operate in an AEMFC), the n value was 4.0 (Fig. 5d), showing that the CST-Pt/NC catalyst was both active and selective.

The sluggish kinetics of the HOR in alkaline media is a significant challenge for developing new catalysts [40,46], and it has limited the development of PGM-free catalysts. Therefore, unlike the ORR where PGM-free materials have emerged, lowering the PGM loading of the anode in the AEMFC will likely initially rely solely on the utilization of supported PtRu with a low loading on the support and in the electrodes. For this reason, the HOR activity of CST-PtRu/VC, CST-PtRu/NC, and Com-PtRu/VC catalysts were evaluated. Thin films of the catalysts were deposited onto a glassy carbon RDE and voltammograms were collected at a scan rate of 50 mV s^{-1} in N_2 -saturated 0.1 M KOH electrolyte. Fig. 5e shows cyclic voltammograms for the three catalysts. Significant differences in their electrochemical behavior were observed. The first difference is in the double-layer capacitance, which results from the larger surface area of NC ($800 \text{ m}^2 \text{ g}^{-1}$) vs. VC ($250 \text{ m}^2 \text{ g}^{-1}$) – just like what was observed with ORR. Using the CVs in this regime, the electrochemically active surface area (ECSA) was calculated using Eq. (5) in the Experimental. The ECSA of the CST-PtRu/NC catalyst was 225% more than that of the Com-PtRu/VC and 150% larger than the CST-PtRu/VC (Fig. 5f). The CST derived clusters have different ECSAs, which can be caused by the different pore structure of the support and the ultra-small size of the clusters. The CST clusters are small enough to fit inside the micropores of the VC support. The CST-PtRu clusters on both VC and NC have a similar size distribution (Fig. S2 c and d). Almost 30% of the surface area of the VC support is inside micropores which will be inaccessible due to capillary effects of the water present in the system. However, the NC support is mesoporous and all of the ultrasmall clusters are expected to be accessible throughout the support.

Next, the HOR for CST-PtRu/NC was evaluated in H_2 -saturated 0.1 M KOH at several rotation speeds between 400 RPM and 2500 RPM (Fig. 5g). Its behavior relative to the other catalysts is compared in Fig. 5h at 1600 RPM. It should be noted that the limiting current density at this rotation rate was 2.42 mA cm^{-2} for CST-PtRu/NC, which is very close to the theoretical value for HOR in the alkaline environment [47]. The difference between CST-PtRu/NC and CST-PtRu/VC in Fig. 5h can be explained by the accessibility of the active sites and mesoporosity of the NC support that makes active sites more accessible. The catalytic sites of CST clusters that are in micropores of VC support are not accessible because the fluid inside micropores is stagnant and might not be affected by the external flow caused by different rotation rates. For the same reason, DI-PtRu/VC shows the lowest limiting current density in its polarization curves (Fig. S5b in Supplementary Information). Fig. 5i shows the HOR mass activity of the CST-PtRu/VC, CST-PtRu/NC, and Com-PtRu/VC catalysts where the mass activity was the highest for CST-PtRu/NC, and was directly proportional to the ECSA, showing that the primary advantage of this catalyst was maximizing the number of active sites that were accessible to H_2 in the reacting environment.

3.3. Integration into operating AEMFCs and performance

Fig. 6 presents the initial polarization and power density curves for AEMFCs operating with several catalyst configurations. In all cases, multiple cells were tested and representative data is shown. All cells were operated at 80°C with H_2/O_2 reacting gas feeds. Fig. 6a shows polarization and power density curves for MEAs with the same high loading commercial PtRu anode ($\text{mg}_{\text{PtRu}} \text{ cm}^{-2}$) and three different cathodes: i) 0.6 mg cm^{-2} Com-Pt/VC; ii) 0.05 mg cm^{-2} CST-Pt/NC; and iii) 0.05 mg cm^{-2} CST-Pt/VC. The amount of catalyst used was based on choosing similar carbon loading for all electrodes to keep the electrode thickness similar. The overall carbon loading on all electrodes was between 0.7 and 0.9 mg cm^{-2} . Under these conditions, the AEMFC using the CST-Pt/NC cathode (0.05 mg cm^{-2} Pt) exhibited a very high peak power density of 2.0 W cm^{-2} , which was very close to commercial Com-

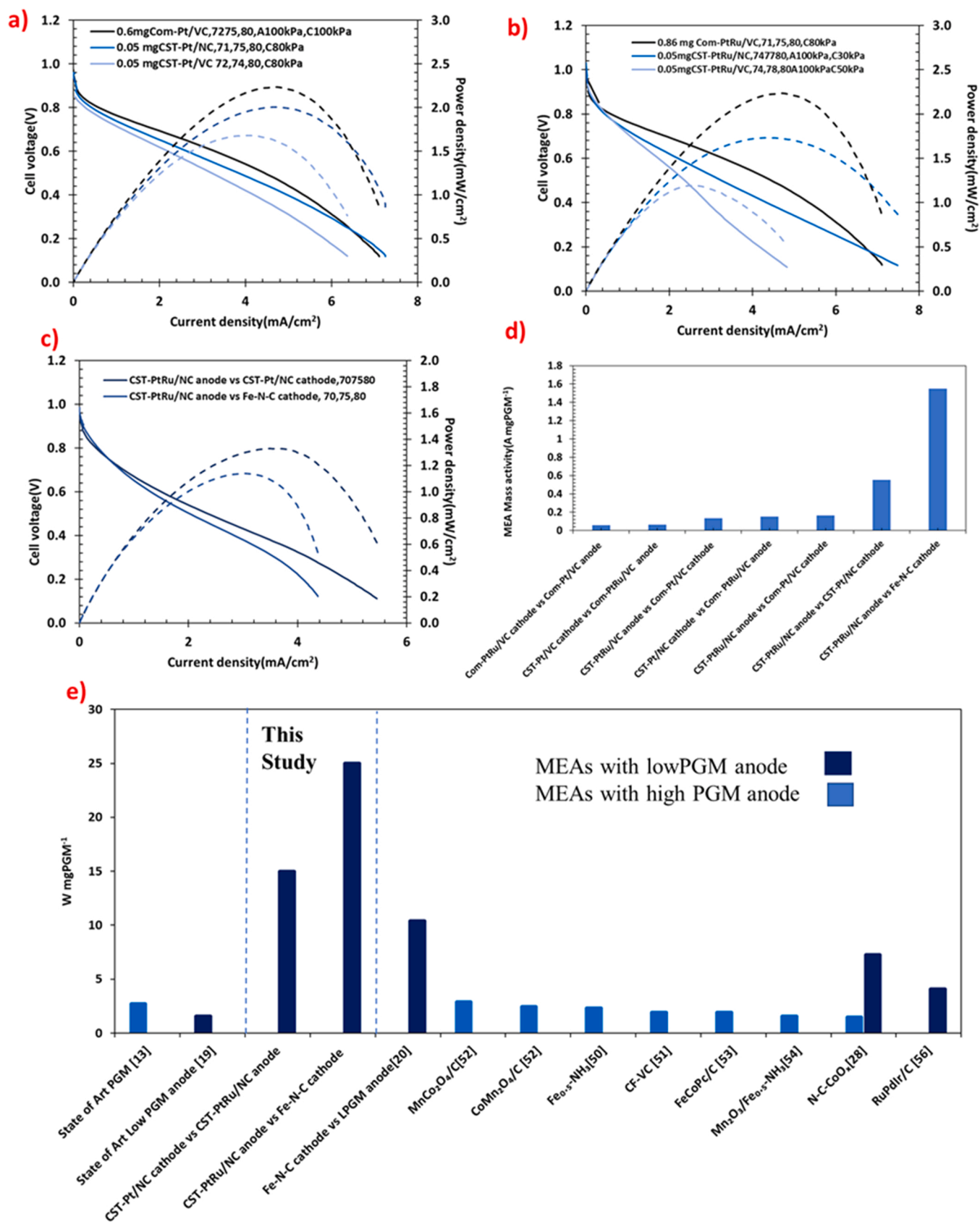
Pt/VC (2.25 W cm^{-2}), despite having only 1/12th of the catalyst loading. The most likely reasons for the high performance at low loading are the much more accessible and high density of active centers (small Pt clusters) as evidenced by the high performance in the low current density kinetic regime even with much less catalyst, as well as the mesoporous structure of the NC support that likely helps with mass transport as indicated by the higher achievable current density at lower potentials.

Fig. 6b shows polarization and power density curves for MEAs with the same high loading commercial Com-Pt/VC cathode ($0.6 \text{ mg}_{\text{Pt}} \text{ cm}^{-2}$) and three different anodes: i) $0.86 \text{ mg}_{\text{PtRu}} \text{ cm}^{-2}$ commercial Com-PtRu/VC; ii) $0.05 \text{ mg}_{\text{PtRu}} \text{ cm}^{-2}$ CST-PtRu/NC; and iii) $0.05 \text{ mg}_{\text{PtRu}} \text{ cm}^{-2}$ CST-PtRu/VC. In short, just like the cathode, much better performance was achieved when the support was switched to NC from VC. The anode with $0.05 \text{ mg}_{\text{PtRu}} \text{ cm}^{-2}$ was able to achieve a peak power density of 1.8 W cm^{-2} , which was approximately 80% of the performance of commercial catalyst with only 1/18th the PGM loading.

Another possible way to compare the CST-PtRu/NC and the commercial catalyst would be to make cells with a similar PtRu loading. There are two ways to do this. One is to make CST electrodes with the same high areal PGM loading as the commercial catalyst in Fig. 6b, but that would negate the entire purpose of this article – to achieve similar performance at much lower loading. Hence, this was not done. The second method would be to use the commercial catalyst and simply make thinner electrodes with the same composition. Previous work from the same academic group writing this paper [55] investigated this approach extensively and it was shown that simply reducing the electrode thickness by half would sacrifice more than 50% of the performance due to increased anode flooding. Reducing it by a factor of 18 (which would be required here) would not only certainly lead to catastrophic flooding and poor performance, but making very thin electrodes that are repeatable and reproducible is also quite challenging. Hence, this was also not done here, but the discussion with worth noting. The best way to compare the catalyst layers without additional changes is to make them with similar thickness (effectively meaning the carbon loading) and compression, and to operate them under similar conditions, which is exactly what was done above.

AEMFCs were assembled with the goal of exceeding the 2022 AEMFC target set forth by the U.S. Department of Energy: initial performance of 0.65 V at 1.0 A cm^{-2} with H_2/O_2 reacting gases, temperature $\geq 80^\circ\text{C}$; pressure $\leq 150 \text{ kPa}$ and total PGM loading $\leq 0.2 \text{ mg cm}^{-2}$. The specific approach here was create cells with very low PGM loading. Fig. 6c shows the results for two configurations. The first one was assembled with GDEs containing 0.05 mg of CST-PtRu/NC on the anode and 0.05 mg of CST-Pt/NC at the cathode (PGM loading of 0.1 mg cm^{-2} , which is one-half of target value). This configuration was able to reach a peak power density of 1.4 W cm^{-2} , translating to a specific power density was $15 \text{ W mg}_{\text{PGM}}^{-1}$ (Fig. 6e), which are both high achievements for a low-PGM AEMFC. The second configuration sought even lower total PGM loading, with a $0.05 \text{ mg}_{\text{PGM}} \text{ cm}^{-2}$ anode combined with a PGM-free Fe-N-C at the cathode. The cathode was chosen to be PGM free because not only has our team had success in the past with deploying Fe-N-C in AEMFCs [13, 29], the data in Fig. 6 suggested that the anode suffered more as the PGM loading was reduced than the cathode (most likely due to high water content at that electrode [2,48,49]). In this configuration, CST-PtRu/NC at the anode and Fe-N-C [29] at the cathode, AEMFCs were able to achieve a peak power density of 1.2 W cm^{-2} and a specific power density of $25 \text{ W mg}_{\text{PGM}}^{-1}$. This number is twice as large as the previous number reported for AEMFCs and also is bigger than the present state-of-the-art for commercialized PEMFCs ($16 \text{ W mg}_{\text{PGM}}^{-1}$). Also both cell configurations in Fig. 6d were able to meet DOE's target for 2022 at steady state (data provided in Supplementary Information Figs. S6 and S7), a significant achievement for the technology.

Fig. 6d shows the overall mass activity (A/mg_{PGM}) of various MEA configurations presented in this study at 0.9 V . The MEA assembled with a Com-Pt/VC cathode and Com-PtRu/VC anode showed the lowest overall mass activity ($0.05 \text{ A mg}_{\text{PGM}}^{-1}$), though highest performance.



(caption on next page)

Fig. 6. AEMFC results with CST and Com catalysts. a) H_2/O_2 AEMFC voltage vs. current density (solid) and power density vs. current density (dash) curves for three MEAs. The anode was 0.86 mg cm^{-2} of Com-PtRu/VC and the cathode was either 0.05 mg cm^{-2} CST-Pt/NC, 0.05 mg cm^{-2} CST-Pt/VC or 0.6 mg Pt cm^{-2} Com-Pt/VC. The cell was operated at 80°C under H_2/O_2 flows of 1.0 L min^{-1} . b) H_2/O_2 AEMFC voltage vs. current density (solid) and power density vs. current density (dash) curves for three MEAs. The cathode was 0.6 mg cm^{-2} Com-Pt/VC and the anode either 0.05 mg cm^{-2} CST-PtRu/NC, 0.05 mg cm^{-2} CST-PtRu/VC or $0.86\text{ mg Pt cm}^{-2}$ Com-PtRu/VC. c) Current-voltage (solid) and current-power density (dash) curves for AEMFC, which assembled with for H_2/O_2 fuel cells; cathode: either 0.05 mg cm^{-2} of CST Pt/NC or 1.0 mg cm^{-2} of Fe-N-C; anode: 0.05 mg cm^{-2} of CST PtRu/NC. d) Overall mass activity at 0.9 V for CST-Pt/VC, CST-Pt/NC, CST-PtRu/NC, CST-PtRu/VC, Com-Pt/VC and PtRu/VC. e) Specific peak power density between this work to the following prior reported PGM-free cathodes: $\text{Fe}_{0.5}\text{-NH}_3$ [50], CF-VC[51], $\text{CoMn}_2\text{O}_4/\text{C}$ [52], $\text{MnCo}_2\text{O}_4/\text{C}$ [52], FeCoPc/C [53], N-C- CO_x [28], $\text{Mn}_2\text{O}_3/\text{Fe}_{0.5}\text{-NH}_3$ [54]; PFe-N-C[29], note that in legend the numbers represent the anode dewpoint, cathode dewpoint and cell temperature, respectively. For example, 70,75,80 means anode temperature is 70°C , cathode temperature is 75°C , and cell temperature is 80°C .

Shifting to CST catalysts in both the anode and cathode improved the overall mass activity of the MEAs. The configuration with CST Pt/NC as cathode and CST-PtRu/NC as anode show very high mass activity ($0.6\text{ A mg}_{\text{Pt}}^{-1}$). However, the highest overall mass activity was achieved with the Fe-N-C cathode and ultra-low PGM anode ($1.6\text{ A mg}_{\text{Pt}}^{-1}$). These last two configurations also show very high specific power density (Fig. 6e), which directly relate to the cost in fuel cell systems.

Lastly, to test CST catalyst durability, cells were assembled with CST-Pt/NC at the cathode and Com-PtRu/VC at the anode. The catalyst loading at the cathode was $0.05\text{ mg}_{\text{Pt}}\text{ cm}^{-2}$. This catalyst was selected because it is known that the ORR cathode is the more harsh environment in low temperature fuel cells due to its higher potential and oxidizing environment. The result is shown in Fig. S8 where an experiment was run for over 100 h. The vertical lines in the plot are times where the cell was stopped to collect intermediate polarization curves, which were very similar to the initial curve. The voltage loss during this time was only 25 mV, showing that the achieved in-cell activity of the small cluster CST catalysts is very temporally stable.

4. Conclusions

This study introduced a new, simple, scalable controlled surface tension (CST) method to synthesize low-PGM catalysts for AEMFCs. The CST method allowed for a high density of well-dispersed multi atom Pt and PtRu clusters. These materials were characterized using a wide array of techniques, including x-ray diffraction (XRD), transmission electron microscopy (TEM), high-resolution Cs aberration-corrected scanning transmission electron microscopy (STEM). They were also tested for their hydrogen oxidation reaction (HOR) and oxygen reduction reaction (ORR) activity and their in-situ behavior in operating AEMFCs. With this new generation of low-PGM materials, it was possible to reduce the PGM loading by a factor of 14 while achieving comparable performance to commercial catalysts. It was shown that the anode side of the AEMFC was the most negatively affected by the removal of the PGM catalysts, so one promising method to reduce the PGM loading is to pair PGM-free cathodes with low-PGM-loading anodes. Pairing CST PtRu/NC anodes were paired with Fe-N-C cathodes which allowed for the demonstration of cells with a specific power of 25 W per mg PGM (40 W per mg Pt). These cells were also able to achieve the DOE 2022 AEMFC target for initial performance.

CRediT authorship contribution statement

Horie Adabi and Abolfazl Shakouri developed the catalyst synthesis method. Horie Adabi did the electrochemical testing. Abolfazl Shakouri did the catalyst characterization. Horie Adabi and Jasmine Bohannon performed the fuel cell testing. Andrea Zitolo and Tristan Asset directed the x-ray absorption measurements and were assisted in their collection by Anastasiya Khan and Raphaël Chattot. Frédéric Jaouen directed the Fe-N-C catalyst synthesis and characterization. Christopher Williams and John R. Regalbutto oversaw the Pt and PtRu catalyst development and characterization. William E. Mustain oversaw the project. Horie Adabi, Abolfazl Shakouri and William E. Mustain were the primary writers and editors of the manuscript.

Declaration of Competing Interest

The authors declare that they have no known competing financial interests or personal relationships that could have appeared to influence the work reported in this paper.

Data availability

Data will be made available on request.

Acknowledgments

HA, JB, and WEM would like to acknowledge the United States Department of Energy Office of Energy Efficiency & Renewable Energy award number DE-EE0008433 for financial support, which enabled the electrochemical testing. A.S. JRR and CW would like to acknowledge funding from United States Army Research Office Contract # W911NF-20-1-0318, which supported the catalyst synthesis and characterization. To support the XAS measurements, the authors acknowledge support from the French ANR project ANR-19-CE05-0006 (SPECTROSCOPE).

Appendix A. Supporting information

Supplementary data associated with this article can be found in the online version at doi:10.1016/j.apcatb.2023.122375.

References

- [1] Y. Wang, G. Wang, G. Li, B. Huang, J. Pan, Q. Liu, J. Han, L. Xiao, J. Lu, L. Zhuang, Pt-Ru catalyzed hydrogen oxidation in alkaline media: oxophilic effect or electronic effect? *Energy Environ. Sci.* 8 (2015) 177–181.
- [2] T.J. Omasta, A.M. Park, J.M. LaManna, Y. Zhang, X. Peng, L. Wang, D.L. Jacobson, J.R. Varcoe, D.S. Hussey, B.S. Pivovar, W.E. Mustain, Beyond catalysis and membranes: visualizing and solving the challenge of electrode water accumulation and flooding in AEMFCs, *Energy Environ. Sci.* 11 (2018) 551–558, <https://doi.org/10.1039/C8EE00122G>.
- [3] G. Huang, M. Mandal, X. Peng, A.C. Yang-Neyerlin, B.S. Pivovar, W.E. Mustain, P. A. Kohl, Composite poly(norbornene) anion conducting membranes for achieving durability, water management and high power (3.4 W cm^{-2}) in hydrogen/oxygen alkaline fuel cells, *J. Electrochem. Soc.* 166 (2019) F637–F644, <http://jes.ecsdl.org/content/166/10/F637.abstract>.
- [4] L. Wang, X. Peng, W.E. Mustain, J.R. Varcoe, Radiation-grafted anion-exchange membranes: the switch from low-to high-density polyethylene leads to remarkably enhanced fuel cell performance, *Energy Environ. Sci.* 12 (2019) 1575–1579.
- [5] S. Maurya, S. Noh, I. Matanovic, E.J. Park, C.N. Villarrubia, U. Martinez, J. Han, C. Bae, Y.S. Kim, Rational design of polyaromatic ionomers for alkaline membrane fuel cells with $> 1\text{ W cm}^{-2}$ power density, *Energy Environ. Sci.* 11 (2018) 3283–3291.
- [6] T. Wang, L. Shi, J. Wang, Y. Zhao, B.P. Setzler, S. Rojas-Carbonell, Y. Yan, High-performance hydroxide exchange membrane fuel cells through optimization of relative humidity, backpressure and catalyst selection, *J. Electrochem. Soc.* 166 (2019) F3305–F3310.
- [7] Q. Li, H. Peng, Y. Wang, L. Xiao, J. Lu, L. Zhuang, The comparability of Pt to Pt-Ru in catalyzing the hydrogen oxidation reaction for alkaline polymer electrolyte fuel cells operated at 80°C , *Angew. Chem. Int. Ed.* 58 (2019) 1442–1446, <https://doi.org/10.1002/anie.201812662>.
- [8] M. Mandal, G. Huang, N.U. Hassan, X. Peng, T. Gu, A.H. Brooks-Starks, B. Bahar, W.E. Mustain, P.A. Kohl, The importance of water transport in high conductivity and high-power alkaline fuel cells, *J. Electrochem. Soc.* 167 (2020), <http://jes.ecsdl.org/content/167/5/054501.abstract>.
- [9] N. Ul Hassan, M. Mandal, G. Huang, H.A. Firouzjaie, P.A. Kohl, W.E. Mustain, Achieving high-performance and 2000h stability in anion exchange membrane fuel

- cells by manipulating ionomer properties and electrode optimization, *Adv. Energy Mater.* N/a (2020), 2001986, <https://doi.org/10.1002/aenm.202001986>.
- [10] B.P. Setzler, Z. Zhuang, J.A. Wittkopf, Y. Yan, Activity targets for nanostructured platinum-group-metal-free catalysts in hydroxide exchange membrane fuel cells, *Nat. Nanotechnol.* 11 (2016) 1020, <https://doi.org/10.1038/nnano.2016.265>.
 - [11] J. Greeley, I.E.L. Stephens, A.S. Bondarenko, T.P. Johansson, H.A. Hansen, T. F. Jaramillo, I. Chorkendorff, J.K. Nørskov, Alloys of platinum and early transition metals as oxygen reduction electrocatalysts, *Nat. Chem.* 1 (2009) 552–556, <https://doi.org/10.1038/nchem.367>.
 - [12] W. Sheng, H.A. Gasteiger, Y. Shao-Horn, Hydrogen oxidation and evolution reaction kinetics on platinum: acid vs alkaline electrolytes, *J. Electrochem. Soc.* 157 (2010) B1529–B1536.
 - [13] H. Adabi, P.G. Santori, A. Shakouri, X. Peng, K. Yassin, I.G. Rasin, S. Brandon, D. R. Dekel, N.U. Hassan, M.-T. Sougrati, A. Zitolo, J.R. Varcoe, J.R. Regalbuto, F. Jaouen, W.E. Mustain, Understanding how single-atom site density drives the performance and durability of PGM-free Fe–N–C cathodes in anion exchange membrane fuel cells, *Mater. Today Adv.* 12 (2021), 100179, <https://doi.org/10.1016/j.mtdadv.2021.100179>.
 - [14] H. Adabi, A. Shakouri, N. Ul Hassan, J.R. Varcoe, B. Zulevi, A. Serov, J. R. Regalbuto, W.E. Mustain, High-performing commercial Fe–N–C cathode electrocatalyst for anion-exchange membrane fuel cells, *Nat. Energy* 6 (2021) 834–843, <https://doi.org/10.1038/s41560-021-00878-7>.
 - [15] Y. Wang, Y. Yang, S. Jia, X. Wang, K. Lyu, Y. Peng, H. Zheng, X. Wei, H. Ren, L. Xiao, J. Wang, D.A. Muller, H.D. Abruña, B.J. Hwang, J. Lu, L. Zhuang, Synergistic Mn–Co catalyst outperforms Pt on high-rate oxygen reduction for alkaline polymer electrolyte fuel cells, *Nat. Commun.* 10 (2019) 1506, <https://doi.org/10.1038/s41467-019-09503-4>.
 - [16] H. Adabi Firouzjaie, W.E. Mustain, Catalytic advantages, challenges, and priorities in alkaline membrane fuel cells, *ACS Catal.* 10 (2019) 225–234, <https://doi.org/10.1021/acscatal.9b03892>.
 - [17] T.J. Omasta, Y. Zhang, A.M. Park, X. Peng, B. Pivovar, J.R. Varcoe, W.E. Mustain, Strategies for reducing the PGM loading in high power AEMFC anodes, *J. Electrochem. Soc.* 165 (2018) F710–F717.
 - [18] S.T. Thompson, D. Peterson, D. Ho, D. Papageorgopoulos, Perspective—The Next Decade of AEMFCs: Near-Term Targets to Accelerate Applied R&D, *J. Electrochem. Soc.* 167 (2020) 84514, <https://doi.org/10.1149/1945-7111/ab8c88>.
 - [19] J. Li, Q. Zhou, M. Yue, S. Chen, J. Deng, X. Ping, Y. Li, J. Li, Q. Liao, M. Shao, Z. Wei, Cross-linked multi-atom Pt catalyst for highly efficient oxygen reduction catalysis, *Appl. Catal. B Environ.* 284 (2021), 119728, <https://doi.org/10.1016/j.apcatb.2020.119728>.
 - [20] Z. Song, Y.-N. Zhu, H. Liu, M.N. Banis, L. Zhang, J. Li, K. Doyle-Davis, R. Li, T.-K. Sham, L. Yang, A. Young, G.A. Botton, L.-M. Liu, X. Sun, Engineering the low coordinated Pt single atom to achieve the superior electrocatalytic performance toward oxygen reduction, *Small* 16 (2020), 2003096, <https://doi.org/10.1002/smll.202003096>.
 - [21] A. Wong, Q. Liu, S. Griffin, A. Nicholls, J.R. Regalbuto, Synthesis of ultrasmall, homogeneously alloyed, bimetallic nanoparticles on silica supports, *Science* (80) (2017).
 - [22] E. Breynaert, M. Houleberghs, S. Radhakrishnan, G. Grubel, F. Taulelle, J. A. Martens, Water as a tuneable solvent: a perspective, *Chem. Soc. Rev.* 49 (2020) 2557–2569, <https://doi.org/10.1039/C9CS00545E>.
 - [23] W. Gao, P. Tieu, C. Addiego, Y. Ma, J. Wu, X. Pan, Probing the dynamics of nanoparticle formation from a precursor at atomic resolution, *eau9590*, *Sci. Adv.* 5 (2019), <https://doi.org/10.1126/sciadv.aau9590>.
 - [24] A. Wong, Q. Liu, S. Griffin, A. Nicholls, J.R. Regalbuto, Synthesis of ultrasmall, homogeneously alloyed, bimetallic nanoparticles on silica supports, *Sci.* (80-) 358 (2017) 1427–1430, <https://doi.org/10.1126/science.aao6538>.
 - [25] L. Jiao, J.R. Regalbuto, The synthesis of highly dispersed noble and base metals on silica via strong electrostatic adsorption: I. Amorphous silica, *J. Catal.* 260 (2008) 329–341, <https://doi.org/10.1016/j.jcat.2008.09.022>.
 - [26] R. Tsekov, H.J. Schulze, B. Radoev, P. Letocart, Dynamics of surface waves in wetting films Dedicated to our deceased colleague H. Sonntag (Berlin)1, *Colloid. Surf. A Physicochem. Eng. Asp.* 142 (1998) 287–294, [https://doi.org/10.1016/S0927-7757\(98\)00363-X](https://doi.org/10.1016/S0927-7757(98)00363-X).
 - [27] A. Zitolo, N. Ranjbar-Sahraie, T. Mineva, J. Li, Q. Jia, S. Stamatini, G.F. Harrington, S.M. Lyth, P. Krtíl, S. Mukerjee, E. Fonda, F. Jaouen, Identification of catalytic sites in cobalt-nitrogen-carbon materials for the oxygen reduction reaction, *Nat. Commun.* 8 (2017) 957, <https://doi.org/10.1038/s41467-017-01100-7>.
 - [28] X. Peng, T.J. Omasta, E. Magliocca, L. Wang, J.R. Varcoe, W.E. Mustain, Nitrogen-doped Carbon–CoOx Nanohybrids: A Precious Metal Free Cathode that Exceeds 1.0 W cm^{−2} Peak Power and 100 h Life in Anion-Exchange Membrane Fuel Cells, *Angew. Chem. Int. Ed.* 58 (2019) 1046–1051, <https://doi.org/10.1002/anie.201811099>.
 - [29] W.E.M. Horie and, Abolfazl Adabia, Shakouria, John R. Noor Ul Hassana, Barr Vacoeb, Alexey Zulevic, John R. Serowc, Regalbutoa, High-Performing Commercial Fe–N–C Cathode Electrocatalyst for Anion Exchange Membrane Fuel Cells, *Nat. Energy Reduce* (2021).
 - [30] R. Zhou, Y. Zheng, M. Jaronic, S.-Z. Qiao, Determination of the electron transfer number for the oxygen reduction reaction: from theory to experiment, *ACS Catal.* 6 (2016) 4720–4728, <https://doi.org/10.1021/acscatal.6b01581>.
 - [31] Y. Garsany, O.A. Baturina, K.E. Swider-Lyons, S.S. Kocha, Experimental methods for quantifying the activity of platinum electrocatalysts for the oxygen reduction reaction, 2010.
 - [32] T.J. Omasta, L. Wang, X. Peng, C.A. Lewis, J.R. Varcoe, W.E. Mustain, Importance of balancing membrane and electrode water in anion exchange membrane fuel cells, *J. Power Sources* 375 (2018) 205–213, <https://doi.org/10.1016/j.jpowsour.2017.05.006>.
 - [33] M. Mandal, G. Huang, N.U. Hassan, X. Peng, T. Gu, A.H. Brooks-Starks, B. Bahar, W.E. Mustain, P.A. Kohl, The importance of water transport in high conductivity and high-power alkaline fuel cells, *J. Electrochem. Soc.* 167 (2019) 54501, <https://doi.org/10.1149/2.0022005jes>.
 - [34] L. Wu, B. Ni, R. Chen, C. Shi, P. Sun, T. Chen, Ultrafine PdAu nanoparticles immobilized on amine functionalized carbon black toward fast dehydrogenation of formic acid at room temperature, *Nanoscale Adv.* 1 (2019) 4415–4421, <https://doi.org/10.1039/C9NA00462A>.
 - [35] V. Raghuvver, A. Manthiram, Mesoporous carbon with larger pore diameter as an electrocatalyst support for methanol oxidation, *Electrochem. Solid-State Lett.* 7 (2004) A336, <https://doi.org/10.1149/1.1792264>.
 - [36] M. Borghei, N. Laorcharen, E. Kibena-Pöldsepp, L.-S. Johansson, J. Campbell, E. Kauppinen, K. Tammeveski, O.J. Rojas, Porous N,P-doped carbon from coconut shells with high electrocatalytic activity for oxygen reduction: Alternative to Pt-C for alkaline fuel cells, *Appl. Catal. B Environ.* 204 (2017) 394–402, <https://doi.org/10.1016/j.apcatb.2016.11.029>.
 - [37] T. Varga, G. Ballai, L. Várhelyi, H. Haspel, Á. Kukovecz, Z. Kónya, Co4N/nitrogen-doped graphene: A non-noble metal oxygen reduction electrocatalyst for alkaline fuel cells, *Appl. Catal. B Environ.* 237 (2018) 826–834, <https://doi.org/10.1016/j.apcatb.2018.06.054>.
 - [38] J. Nash, J. Zheng, Y. Wang, B. Xu, Y. Yan, Mechanistic Study of the Hydrogen Oxidation/Evolution Reaction over Bimetallic PtRu Catalysts, *J. Electrochem. Soc.* 165 (2018) J3378–J3383.
 - [39] S. Zhu, X. Qin, F. Xiao, S. Yang, Y. Xu, Z. Tan, J. Li, J. Yan, Q. Chen, M. Chen, M. Shao, The role of ruthenium in improving the kinetics of hydrogen oxidation and evolution reactions of platinum, *Nat. Catal.* 4 (2021) 711–718, <https://doi.org/10.1038/s41929-021-00663-5>.
 - [40] E.S. Davydova, S. Mukerjee, F. Jaouen, D.R. Dekel, Electrocatalysts for hydrogen oxidation reaction in alkaline electrolytes, *ACS Catal.* 8 (2018) 6665–6690, <https://doi.org/10.1021/acscatal.8b00689>.
 - [41] Q. Li, H. Peng, Y. Wang, L. Xiao, J. Lu, L. Zhuang, The comparability of Pt to Pt–Ru in catalyzing the hydrogen oxidation reaction for alkaline polymer electrolyte fuel cells operated at 80 °C, *Angew. Chem. Int. Ed.* 58 (2019) 1442–1446, <https://doi.org/10.1002/anie.201812662>.
 - [42] R. Bavand, A. Korinek, G.A. Botton, A. Yelon, E. Sacher, PtRu Alloy Nanoparticles I. Physicochemical Characterizations of Structures Formed as a Function of the Type of Deposition and Their Evolutions on Annealing, *J. Phys. Chem. C* 121 (2017) 23104–23119, <https://doi.org/10.1021/acs.jpcc.7b04434>.
 - [43] Q. Liu, Z. Zhang, Platinum single-atom catalysts: a comparative review towards effective characterization, *Catal. Sci. Technol.* 9 (2019) 4821–4834, <https://doi.org/10.1039/C9CY01028A>.
 - [44] X. Hu, G. Luo, Q. Zhao, D. Wu, T. Yang, J. Wen, R. Wang, C. Xu, N. Hu, Ru single atoms on N-doped carbon by spatial confinement and ionic substitution strategies for high-performance Li–O₂ batteries, *J. Am. Chem. Soc.* 142 (2020) 16776–16786, <https://doi.org/10.1021/jacs.0c07317>.
 - [45] C. Zhang, J. Sha, H. Fei, M. Liu, S. Yazdi, J. Zhang, Q. Zhong, X. Zou, N. Zhao, H. Yu, Z. Jiang, E. Ringe, B.I. Yakobson, J. Dong, D. Chen, J.M. Tour, Single-atomic ruthenium catalytic sites on nitrogen-doped graphene for oxygen reduction reaction in acidic medium, *ACS Nano* 11 (2017) 6930–6941, <https://doi.org/10.1021/acsnano.7b02148>.
 - [46] Y. Qiu, X. Xie, W. Li, Y. Shao, Electrocatalysts development for hydrogen oxidation reaction in alkaline media: From mechanism understanding to materials design, *Chin. J. Catal.* 42 (2021) 2094–2104, [https://doi.org/10.1016/S1872-2067\(21\)64088-3](https://doi.org/10.1016/S1872-2067(21)64088-3).
 - [47] C.A. Campos-Roldán, R.G. González-Huerta, N. Alonso-Vante, Experimental Protocol for HOR and ORR in Alkaline Electrochemical Measurements, *J. Electrochem. Soc.* 165 (2018) J3001–J3007, <http://jes.ecsdl.org/content/165/15/J3001.abstract>.
 - [48] H. Deng, D. Wang, R. Wang, X. Xie, Y. Yin, Q. Du, K. Jiao, Effect of electrode design and operating condition on performance of hydrogen alkaline membrane fuel cell, *Appl. Energy* 183 (2016) 1272–1278, <https://doi.org/10.1016/j.apenergy.2016.09.091>.
 - [49] X. Peng, D. Kulkarni, Y. Huang, T.J. Omasta, B. Ng, Y. Zheng, L. Wang, J. M. LaManna, D.S. Hussey, J.R. Varcoe, I.V. Zenyuk, W.E. Mustain, Using operando techniques to understand and design high performance and stable alkaline membrane fuel cells, *Nat. Commun.* 11 (2020) 3561, <https://doi.org/10.1038/s41467-020-17370-7>.
 - [50] H.A. Firouzjaie, W.E. Mustain, Catalytic advantages, challenges, and priorities in alkaline membrane fuel cells, *ACS Catal.* 10 (2020) 225–234, <https://doi.org/10.1021/acscatal.9b03892>.
 - [51] X. Peng, V. Kashyap, B. Ng, S. Kurugot, L. Wang, R.J. Varcoe, E.W. Mustain, High-Performing PGM-Free AEMFC Cathodes from Carbon-Supported Cobalt Ferrite Nanoparticles, *Catal* 9 (2019), <https://doi.org/10.3390/catal9030264>.
 - [52] Y. Yang, H. Peng, Y. Xiong, Q. Li, J. Lu, L. Xiao, F.J. DiSalvo, L. Zhuang, H. D. Abruña, High-Loading Composition-Tolerant Co–Mn Spinel Oxides with Performance beyond 1 W cm^{−2} in Alkaline Polymer Electrolyte Fuel Cells, *ACS Energy Lett.* 4 (2019) 1251–1257, <https://doi.org/10.1021/acsenergylett.9b00597>.
 - [53] L. Wang, M. Bellini, H.A. Miller, J.R. Varcoe, A high conductivity ultrathin anion-exchange membrane with 500+ h alkali stability for use in alkaline membrane fuel

- cells that can achieve 2 W cm⁻² at 80 °C, J. Mater. Chem. A 6 (2018) 15404–15412, <https://doi.org/10.1039/C8TA04783A>.
- [54] P.G. Santori, F.D. Speck, S. Cherevko, H.A. Firouzjaie, X. Peng, W.E. Mustain, F. Jaouen, High Performance FeNC and Mn-oxide/FeNC Layers for AEMFC Cathodes, J. Electrochem. Soc. 167 (2020), 134505, <https://doi.org/10.1149/1945-7111/abb7e0>.
- [55] T.J. Omasta, Y. Zhang, A.M. Park, X. Peng, B. Pivovar, J.R. Varcoe, W.E. Mustain, Strategies for Reducing the PGM Loading in High Power AEMFC Anodes, J. Electrochem. Soc. 165 (2018) F710–F717.